The apparent activation energy and pre-exponential kinetic factor for heterogeneous calcium carbonate nucleation on quartz

Qingyun Li[1] & Young-Shin Jun[1]

Nucleation occurs widely in materials synthesis and natural environments. However, in the nucleation rate equation, values for the apparent activation energy (E_a) and the pre-exponential kinetic factor (A) are thus far unknown because real-time nanoscale observations are difficult to perform. Here we experimentally determine E_a and A using heterogeneous calcium carbonate nucleation on quartz as a model system. Nucleation rates are measured with in situ grazing incidence small-angle X-ray scattering and ex situ atomic force microscopy, and the experiments are conducted with a fixed supersaturation of $IAP/K_{sp}(calc) = 10^{1.65}$ at 12, 25, and 31 °C. E_a is calculated as 45 ± 7 kJ mol^{-1}, and A is $10^{12.0 \pm 1.1}$ nuclei μm^{-2} min^{-1}, or $10^{2.9 \pm 1.3}$ mol m^{-2} min^{-1}. Increasing the temperature shortens the induction time, but does not change nucleus sizes. These parameter values are critical for predicting and controlling the nucleation of materials.

[1] Department of Energy, Environmental & Chemical Engineering, Washington University in St. Louis, St. Louis, MO 63130, USA. Correspondence and requests for materials should be addressed to Y.-S.J. (email: ysjun@seas.wustl.edu)

Nucleation is the first step of forming a stable new phase from a supersaturated medium. In this manuscript we focus on the nucleation of a solid phase from a supersaturated liquid solution. During the nucleation process, the smallest possible units of the solid phase, called nuclei, form in a supersaturated solution. These nuclei then evolve by growth, ripening, aggregation and agglomeration, phase transformation, and crystallization. The nucleation process, especially when it occurs at interfaces (i.e., heterogeneous nucleation), is both profoundly important and widely encountered in material synthesis[1–6], battery operation[7–9], cement hardening[10,11], geochemistry[2,12–14], geologic CO_2 sequestration[15], biomineralization[16,17], industrial scaling control[18,19], and drug production[20]. Understanding nucleation and quantifying the related thermodynamic and kinetic parameters are prerequisites for comprehensively describing, predicting, controlling, and fine tuning these systems.

In current numerical models that include solid phase formation, nucleation is usually approximated by precipitation on seeds of the secondary phase because the parameters required for numerically simulating nucleation process is lacking. However, the seeded model can miss important characteristics of nucleation, such as the high specific reactive surface area of nuclei and the rate-limiting role of nucleation[14,21]. To incorporate nucleation into simulations, we need a deeper understanding of its kinetic and thermodynamic parameters[21–24].

An effective way of describing nucleation is presented by the nucleation rate equation:

$$J = J_0 \exp\left(-\frac{\Delta G^*}{RT}\right) = A\exp\left(-\frac{E_a}{RT}\right)\exp\left(-\frac{\Delta G^*}{RT}\right), \quad (1)$$

in which J is the nucleation rate with the unit of number, volume, or monomer-consumption $cm^{-3}\,s^{-1}$ for homogeneous nucleation, or number, volume, or monomer-consumption $cm^{-2}\,s^{-1}$ for heterogeneous nucleation. R is the ideal gas constant ($8.3144598\,J\,mol^{-1}\,K^{-1}$), T is temperature in Kelvin (K), and ΔG^* is the thermodynamic energy barrier ($J\,mol^{-1}$) which is related to interfacial energies. J_0 in Eq. (1) is attributed to the kinetics of the system, and can be expanded into $\exp\left(-\frac{E_a}{RT}\right)$ (refs. [25–28]), where A is the pre-exponential kinetic factor related to ion diffusion and nuclei surface properties, and E_a is the apparent activation energy ($J\,mol^{-1}$) and therefore is the kinetic energy barrier. The mathematical derivation of Eq. (1) is based on an imagined pathway where nuclei are formed by addition of one monomer at a time, until the size of the nucleus is large enough to stabilize the nucleus as a new phase[29]. Despite the discovery of more realistic nucleation pathways in the past decade[17,30–32], Eq. (1) has been found to be able to repeatedly capture nucleation kinetics[25,31,33–37], and therefore can serve as an effective description in numerical models for evaluation and prediction of nucleation.

Until now, a comprehensive understanding of nucleation has been hindered by limited knowledge of both the thermodynamic and kinetic factors in Eq. (1), except for commonly used solubility products (K_{sp}) and mass densities. With regard to thermodynamic parameters, the interfacial energies have been reported for several common materials[29,38]. For example, Fernandez-Martinez et al.[34] and Li et al.[36] reported that the interfacial energies for nucleation of $CaCO_3$ on silicates were as low as $35–50\,mJ\,m^{-2}$. The overall system's interfacial energy can be affected appreciably by individual interfacial energies among nuclei, substrates, and solutions[13,33,35,36,39–41].

The kinetic parameters in Eq. (1), however, are surprisingly less known. Because information on J_0 is lacking, most previous studies have assumed a constant J_0 term[25,33,34]. To the authors' knowledge, investigations of J_0 are limited to one theoretical estimation and one experimental study at room temperature: Nielsen (1964)[28] estimated J_0 for homogeneous nucleation to be $D/5d$, where D is the diffusion coefficient of the monomers and d is the monomer diameter, and Wallace et al. reported J_0 obtained from a in situ atomic force microscope (AFM) for silica nucleation on carboxyl and NH_3^+/COO^--hybrid substrates to be $10^{13.5 \pm 0.7}$ and $10^{14.8 \pm 1.4}$ nuclei $m^{-2}\,min^{-1}$, respectively. However, the range of J_0 for other systems is seriously lacking, and there is no experimental quantification that leads to reliable estimation under various temperatures.

The lack of efforts to pursue J_0 is partially attributed to the assumption that J_0 is less influential for nucleation rates than are interfacial energies[28], although two studies have already provided evidence that J_0 alone can account for more than a 10-fold difference in the nucleation rate under certain conditions[1,42]. The importance of J_0 brought up the necessity of quantifying E_a and A in order to calculate J_0 and to predict the nucleation process reliably in order to fine-tune nucleation systems efficiently either by modifying interfacial energies or by altering kinetic barriers.

Here we describe an experimental study that uses in situ grazing incidence small-angle X-ray scattering (GISAXS) and ex situ AFM to determine E_a and A for more accurate estimation of J_0 in Eq. (1) under different conditions. Heterogeneous $CaCO_3$ nucleation at a water–quartz interface (12–31 °C, $IAP/K_{sp(calcite)} = 10^{1.65}$) is employed as a model system, because this system involves two of the most common materials in natural and engineered systems, and because interfacial energies have been reported for exactly the same experimental setup[36], so that system errors are minimized. The calculations result in an apparent activation energy E_a of $45 \pm 7\,kJ\,mol^{-1}$ and a pre-exponential kinetic factor A of $10^{12.0 \pm 1.1}$ nuclei $\times$ (μm^{-2} of quartz substrate surface area) $\times$ min^{-1}, or $10^{2.9 \pm 1.3}$ (moles of Ca^{2+} or CO_3^{2-} consumed from the solution) $\times$ (m^{-2} of quartz substrate surface area) $\times$ min^{-1}. The values for E_a and A can be directly applied to numerical models to simulate and optimize the targeted system, and the GISAXS-AFM methods developed in this study can be adapted to general systems that utilize GISAXS at interfaces.

Results

Apparent activation energy. Background-subtracted X-ray scattering intensities from heterogeneously formed $CaCO_3$ nuclei are shown in Fig. 1. From numerical fitting of the GISAXS intensity as stated in the section "Methods", we observed that under all the conditions, the radii of the nuclei were 4.7 ± 0.7 nm, without significant difference. Nucleus growth was not appreciable, and therefore the system was nucleation-dominant.

The nucleus numbers in relative units (r.u.) obtained from GISAXS are plotted versus reaction times in Fig. 2. Nucleus numbers (r.u.) were extracted from two methods (as described in Methods): the invariant method, which assumes that nucleation is dominant over particle growth, plotted on the left axis; and the GISAXS intensity fitting method, which deconvolutes nucleation from particle growth but requires relatively high signal-to-noise ratios, plotted on the right axis. The results from the two methods are consistent with each other (i.e., they overlap for most parts) after appropriate linear scaling of the y-axes. Therefore, for early time points where the signal-to-noise ratio is too low to be fitted with the GISAXS intensity model, the invariant values can be used to forecast the trend of data from GISAXS fitting. The slopes from the linear regressions of the GISAXS-obtained nucleus numbers (r.u.) over reaction time were taken as nucleation rates (r.u.), because, unlike the invariant method which is influenced by particle growth (see Supplementary Figure 1), the fitting method can separate nucleation from nucleus growth (although not
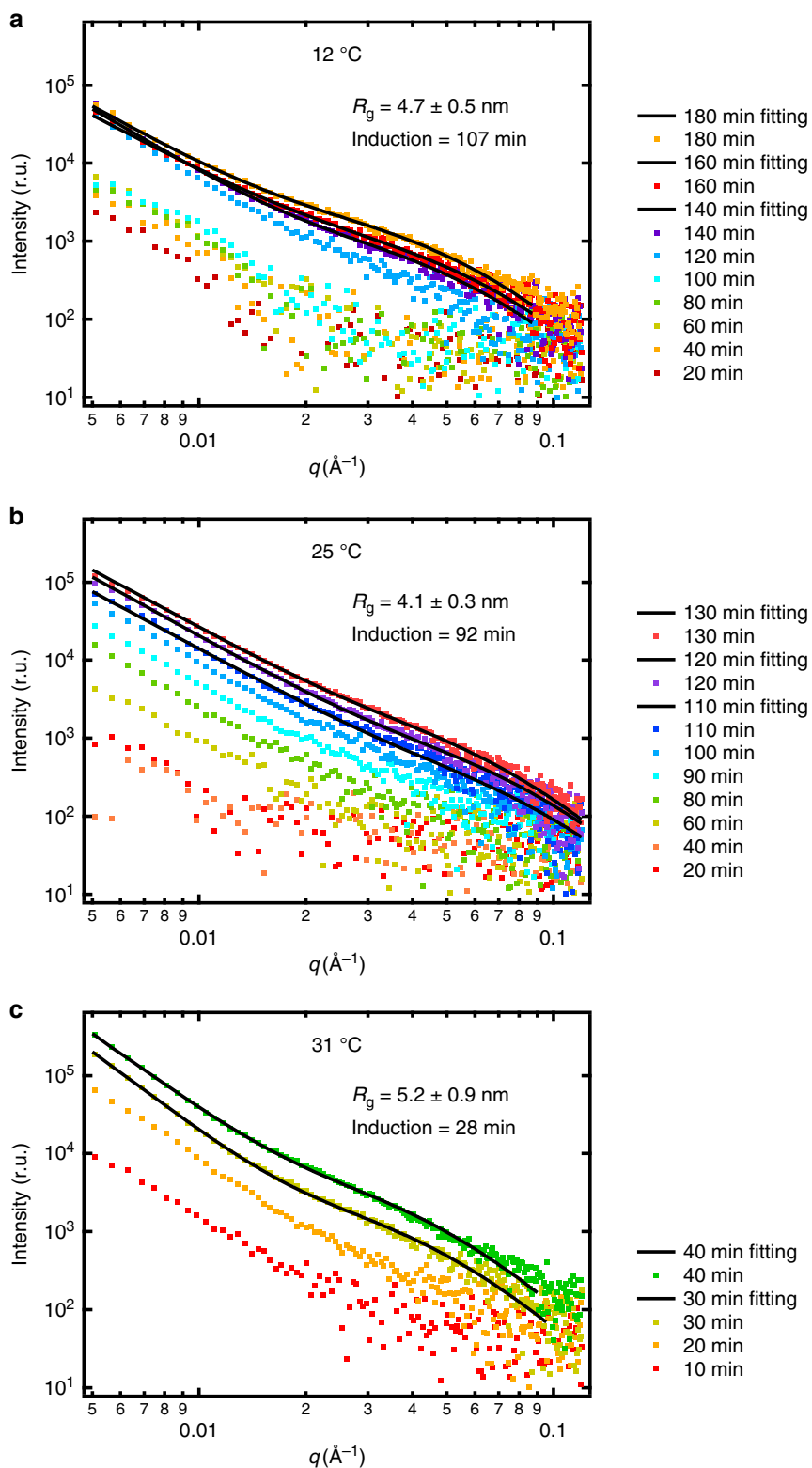
Fig. 1 Plots of background-subtracted scattering intensities over the scattering vector q at selected time points. Panels **a–c** are for 12, 25, and 31 °C systems, respectively. The data points at q higher than ~0.1 Å have low signal-to-noise ratios and are not considered in data analyses. Radii of gyration R_g were obtained from GISAXS intensity fitting, and did not evolve appreciably with time under all conditions. In all systems, the GISAXS intensity fitting shows similar nucleus sizes. The higher the temperature, the faster the nucleation and the shorter the induction time
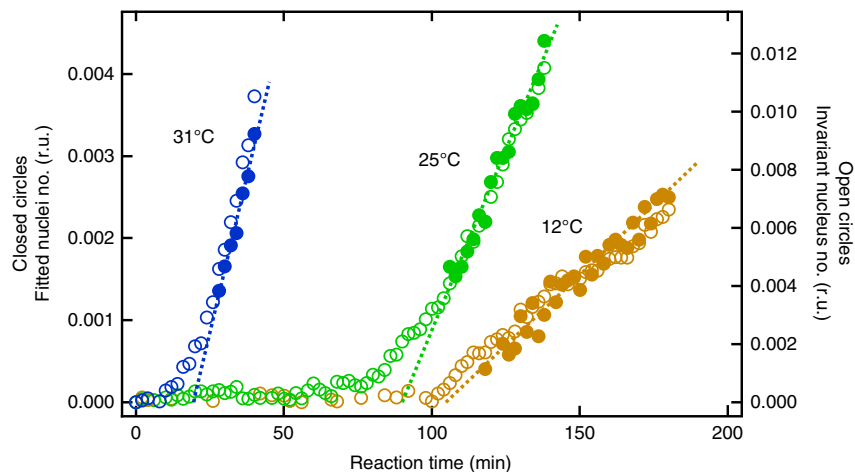
Fig. 2 Representative plots of invariant values and fitted nuclei numbers with respect to reaction times. Invariant values are plotted in open circles, and the fitted nucleus numbers are plotted in closed circles. The relative unit on the left axis is not the same with that on the right axis. The dotted lines are from linear regressions of the fitted nucleus numbers over reaction times. The slopes of these regressed lines are taken as the nucleation rates, J
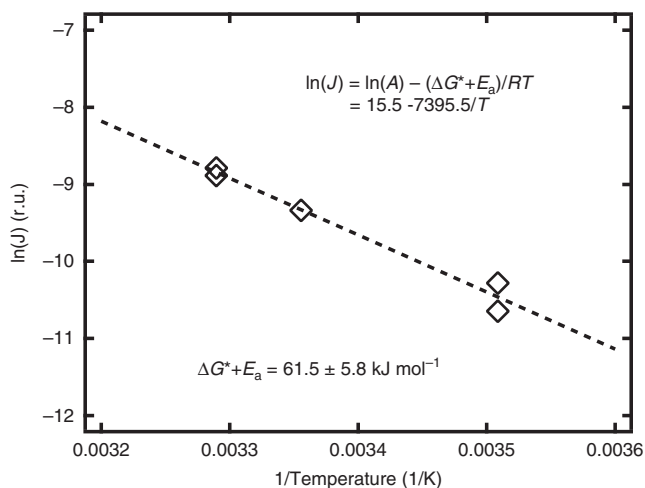

Fig. 3 Plot of $\ln(J)$ versus $1/T$. The linear regression yields a R^2 of 0.9741, and the resulting slope is used to calculate the sum of $(\Delta G^* + E_a)$

noticeable in our systems) and is considered more accurate. The intersection of the regressed lines with the x-axis were taken as the induction times. The logarithms of these nucleation rates were regressed over $1/T$, as shown in Fig. 3, according to a rearrangement of Eq. (1):

$$\ln(J) = \ln(A) - \frac{\Delta G^* + E_a}{RT}. \qquad (2)$$

The resulting $\Delta G^* + E_a$ was 61.5 ± 5.8 kJ mol^{-1}. To obtain E_a, the value of ΔG^* was calculated according to

$$\Delta G^* = \frac{16\pi v^2 \alpha^3}{3R^2 T^2 \left[\ln\left(\frac{\text{IAP}}{K_{sp}}\right)\right]^2}. \qquad (3)$$

In Eq. (3), v is the molar volume of nuclei (cm^3 mol^{-1}) and can be estimated using the density and molecular weight of the nucleating material. The constant $16\pi/3$ is a geometry factor from the mathematical derivation for homogeneous nucleation of

spherical particles[29], with α representing the interfacial energy between nuclei and fluid. However, note that for heterogeneous nucleation, $16\pi/3$ is no longer a geometry factor but becomes a numerical constant. It is used in the heterogeneous nucleation case not to suggest spherical nuclei, but to facilitate comparison between the interfacial energy in homogeneous nucleation and the effective interfacial energy in heterogeneous nucleation. The complex relationship among the nuclei geometry, contact angle of nuclei on substrates, and the interfacial energies among nuclei, substrate, and liquid is accounted for in α, the effective interfacial energy of the system. In our previous studies, the α at room temperature for CaCO$_3$ nucleation on quartz was experimentally found to be 47.1 ± 1.3 mJ m^{-2}(refs. [1,36]). IAP is the ion activity product (Ca^{2+})(CO$_3^{2-}$), and K_{sp} is the solubility product of the nucleating CaCO$_3$ phase. In this study, the reaction solutions were supersaturated with calcite and vaterite, and were undersaturated with amorphous CaCO$_3$. To avoid unnecessary complication with CaCO$_3$ phase transformation and to serve as a direct reference for numerical models where calcite is included as the CaCO$_3$ phase, our calculation used v and K_{sp} for calcite. Calculations for vaterite can be found in Supplementary Note 1 and Supplementary Table 1. With these parameters, the thermodynamic energy barrier, ΔG^*, was calculated as 16 ± 3 kJ mol^{-1} in the temperature range of 12–31 °C (15.5 ± 1.3 kJ mol^{-1} for 12 °C, 16.2 ± 1.3 kJ mol^{-1} for 25 °C, and 18.6 ± 1.5 kJ mol^{-1} for 31 °C). Subtraction of ΔG^* from the sum of $(\Delta G^* + E_a)$ gave the kinetic energy barrier, E_a, equal to 45 ± 7 kJ mol^{-1}.

Pre-exponential kinetic factor. For nucleating materials with high scattering length density and in vacuum or an air background, the high signal-to-noise ratio of GISAXS signals can be numerically fitted with geometrical modeling[43]. On the other hand, for nucleation in liquid systems, especially those where water acts as a reaction medium, the GISAXS signals after background subtraction are typically low and often do not support geometrical modeling. In these cases, the absolute nucleus numbers can be achieved by straightforward calibration of GISAXS data with AFM images. Representative AFM images of heterogeneously formed nuclei are shown in Fig. 4. Large particles were homogeneously formed and settled on the substrate, and were not the focus of this study. Small particles were heterogeneously formed and evenly distributed over the whole substrate (also see Supplementary Figure 2). These small nuclei were
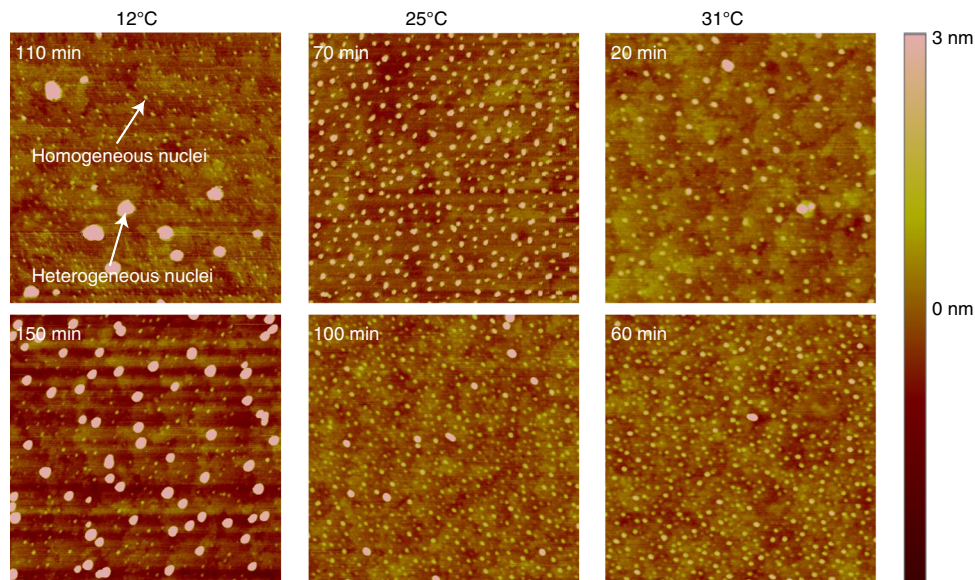
Fig. 4 Representative AFM images of nuclei formed at different temperatures. Each image is a $1 \times 1\,\mu m^2$ area. The evenly distributed particles formed heterogeneously, while the larger particles formed homogeneously and settled to the quartz substrate surface
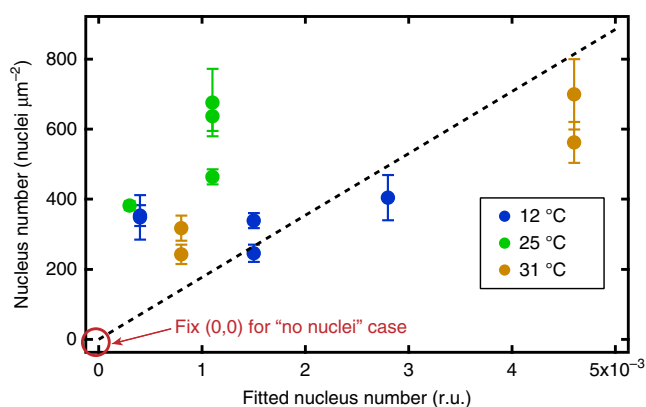

Fig. 5 Calibration of GISAXS results with AFM imaging. The nucleus numbers counted from AFM images with units of nuclei μm^{-2} are plotted versus the nucleus numbers in relative units obtained from fitting the GISAXS data. Error bars for the data points are particle number deviations from three $1 \times 1\,\mu m^2$ scan areas on a single substrate. The linear fitting line is known to cross (0,0), where no nuclei were formed on substrate, and no GISAXS signal should be observed. The correction factor from x-axis values to y-axis values is $(1.77 \pm 0.35) \times 10^5$

manually counted within a unit area of one square micrometer. The GISAXS-obtained particle numbers (r.u.) under the same conditions and at the same reaction time can be read from Fig. 2 on the right y-axis. Fig. 5 plots nuclei numbers counted from AFM images versus GISAXS-obtained nuclei numbers (r.u.). Each data point in Fig. 5 was generated from at least three $1\,\mu m^2$ areas within one piece of quartz substrate. The data points in Fig. 5 are scattered because the induction time for 12 °C and 25 °C samples had a typical 20–30 min uncertainty.

In Fig. 5, regression of the particle numbers over the GISAXS-obtained particle numbers (r.u.) intersects at the point (0,0), where no GISAXS signals from nuclei can be observed when there are no nuclei formed on the substrate. This regression provided the correction factor from relative nuclei numbers obtained from

GISAXS intensity fitting to absolute numbers, specifically $(1.77 \pm 0.35) \times 10^5$. Despite the uncertainty introduced by the induction time, the narrow standard deviation of the correction factor indicates the validity of this calibration. The validity is also demonstrated by the fact that the regression, obtained from all the data points, well captures the data points with the least uncertainty in induction time (i.e., data at 31 °C). With this correction factor, the nucleation rates from GISAXS data were corrected from relative units to absolute units of nuclei $\mu m^{-2}\,min^{-1}$ (Table 1). The absolute value of the pre-exponential kinetic factor, A, can also be calculated in a similar way, according to the regression result $(\ln(A) = 15.5 \pm 2.4)$ shown in Fig. 3. The value of A is 9.4×10^{11} nuclei $\mu m^{-2}\,min^{-1}$, or 1.6×10^{22} nuclei $m^{-2}\,s^{-1}$, with one order of magnitude uncertainty.

To compare with J_0 values ($10^{13.5 \pm 0.7}$ and $10^{14.8 \pm 1.4}$ nuclei $m^{-2}\,min^{-1}$ at room temperature) for heterogeneous silica nucleation reported by Wallace et al. (2009), we employed the values of A and E_a obtained in this study and calculated $J_0 = A \exp(-E_a/RT)$ for heterogeneous $CaCO_3$ on clean quartz to be $10^{16.1 \pm 1.0}$ nuclei $m^{-2}\,min^{-1}$ at 25 °C. The higher J_0 for $CaCO_3$ nucleation is consistent with the observation that $CaCO_3$ nucleation is faster than silica nucleation. The comparison provides a sense on the variation of J_0 for different nucleating materials.

Nucleation rates expressed as concentration changes. Because reaction rates in aqueous solutions are often expressed with moles, the convenient unit for nucleation is not the nuclei number per unit area of substrate per unit time (e.g., nuclei μm^{-2} min^{-1}), but moles of the reactant consumed per unit area of substrate per unit time (e.g., mol $\mu m^{-2}\,min^{-1}$). Using the lateral nucleus radius value of 4.7 ± 0.7 nm obtained from GISAXS, the individual nucleus volume was calculated as 34.5 ± 15.4 nm^3. This calculation employs the calculation method and nucleus geometry obtained in our previous study[1,36], where an individual nucleus resembles the top section of an ellipsoid, with a contact angle on quartz <90° and a fixed ratio of nucleus height to lateral radius equal to 1/6. The relative standard deviation of nuclei volumes is expected to be reduced for materials that generate larger nuclei,

5

Table 1 Nucleation rates and pre-exponential kinetic factors obtained in this study expressed in different units

Temperature and pre-exponential kinetic factor	Fitted nucleation rate ($r.u.\ min^{-1}$)	Absolute nucleation rate (nuclei $\mu m^{-2}\ min^{-1}$)	Absolute nucleation rate ($nm^3\ \mu m^{-2}\ min^{-1}$)	Absolute nucleation rate ($mol\ m^{-2}\ min^{-1}$)
12 °C	$(3.4 \pm 0.1) \times 10^{-5}$	6.0 ± 1.2	$(2.1 \pm 1.0) \times 10^2$	$(5.6 \pm 2.8) \times 10^{-9}$
25 °C	$(8.8 \pm 0.4) \times 10^{-5}$	15.6 ± 3.2	$(5.4 \pm 2.6) \times 10^2$	$(14.5 \pm 7.1) \times 10^{-9}$
31 °C	$(15.0 \pm 1.0) \times 10^{-5}$	26.5 ± 5.6	$(9.2 \pm 4.5) \times 10^2$	$(25 \pm 12) \times 10^{-9}$
A	$10^{6.7 \pm 1.0}$	$10^{12.0 \pm 1.1}$	$10^{13.5 \pm 1.3}$	$10^{2.9 \pm 1.3}$

The error ranges are standard deviations from the experimental data

because dimensions of large nuclei can be measured more accurately. Multiplication of individual nucleus volumes (m^3) and nucleation rates (nuclei $m^{-2}\ s^{-1}$) gives nucleation rates in units of the volume of nuclei per unit area of substrate surface per unit time (i.e., $m^3\ m^{-2}\ s^{-1}$). If the $CaCO_3$ phase is calcite, as commonly used in reactive transport modeling approaches, the moles of Ca^{2+} or CO_3^{2-} ions consumed from the solution can be calculated by dividing the volume nucleation rates ($m^3\ m^{-2}\ s^{-1}$) by the molar volume of calcite ($m^3\ mol^{-1}$), where the molar volume is just the product of the reciprocal of calcite density ($g\ cm^{-3}$) and the molar weight ($g\ mol^{-1}$) of calcite:

$$\nu = \frac{1}{\rho} \times MW. \qquad (4)$$

If the nucleating $CaCO_3$ phase is assumed to be other than calcite, the K_{sp} and molecular volume should correspond to that specific phase, but the methods for obtaining E_a and A are the same as presented for calcite. The results for vaterite are available in Supplementary Note 1 and Supplementary Table 1. The obtained nucleation rate was in moles of Ca^{2+} or CO_3^{2-} ions consumed per unit area of substrate surface per unit time (i.e., $m^3\ m^{-2}\ s^{-1}$). Because the pre-exponential kinetic factor, A, has the same units as the nucleation rate J, the unit conversion method for A is the same as that for J. The calculated values for J and A with different units are shown in Table 1.

For heterogeneous nucleation, the geometry of the nuclei, including the nucleus contact angle on substrates and the ratio of nucleus high to lateral radius, is accounted for by the effective interfacial energy α. Because the α-value of $47\ mJ\ m^{-2}$ used for calculation in this study is obtained from direct observation of $CaCO_3$ on quartz using the same setup and under similar conditions[36], it has already incorporated the information of the nucleus geometry which does not need to be specifically determined. Therefore, there is no need to doubly consider nucleus geometry when calculating A (nuclei $\mu m^{-2}\ min^{-1}$), E_a ($kJ\ mol^{-1}$), and J (nuclei $\mu m^{-2}\ min^{-1}$) using this α-value. However, when converting A and J to units of $nm^3\ \mu m^{-2}\ min^{-1}$ or $mol\ m^{-2}\ min^{-1}$, the geometry of the nuclei will influence the results by affecting the individual nucleus volume. For example, if the ratio of nucleus height to lateral radius doubles from 1/6 to 1/3, the volume of an individual nucleus will increase by 90% from 34.5 ± 15.4 to $65.5 \pm 29.3\ nm^3$, resulting in a 90% increase in the values of A and J with units of $nm^3\ \mu m^{-2}\ min^{-1}$ and $mol\ m^{-2}\ min^{-1}$, while A and J in other units in Table 1 remain unchanged.

Sensitivity analyses for thermodynamic and kinetic factors. The overall energy barrier for nucleation is a combination of the kinetic energy barrier (E_a) and the thermodynamic energy barrier (ΔG^*). ΔG^* is largely determined by supersaturations and interfacial energies, whereas E_a is related to kinetic factors such as the rate of monomer diffusion in solution and on the substrate, the

impingement rate of monomers onto the substrate, and the incorporation rate of monomers into existing nuclei[44]. Because E_a and ΔG^* are both Arrhenius-type energy barriers according to Eq. (1), it has been hard to estimate the nucleation rate as a function of temperature without a reliable E_a value. With E_a quantified, it is now possible to analyze the nucleation rate as a function of temperature. Taking the conditions in this study as an example (Fig. 6a, $\alpha = 47\ mJ\ m^{-2}$, $IAP/K_{sp} = 10^{1.65}$, $E_a = 45\ kJ\ mol^{-1}$, and $\Delta G^*(25\ °C) = 16\ kJ\ mol^{-1}$), the $CaCO_3$ nucleation rate is shown to increase with a decrease in either α or E_a, or an increase in $\log_{10}(IAP/K_{sp})$, according to Eqs. (1) and (3), for the temperature range of 10–50 °C. The amount of change is set to 20% to allow clear comparison. In this case the nucleation rate is effectively enhanced by tuning any of the three parameters. However, for a system with an interfacial energy as low as $30\ mJ\ m^{-2}$ (Fig. 6b, $IAP/K_{sp} = 10^{1.65}$, $E_a = 45\ kJ\ mol^{-1}$, and $\Delta G^*(25\ °C) = 4\ kJ\ mol^{-1}$), further reducing the interfacial energy or enhancing supersaturation does not increase the nucleation rate as effectively as reducing the kinetic barrier (E_a). Conversely, if the interfacial energy is $60\ mJ\ m^{-2}$ (Fig. 6c, $IAP/K_{sp} = 10^{1.65}$, $E_a = 45\ kJ\ mol^{-1}$, and $\Delta G^*(25\ °C) = 34\ kJ\ mol^{-1}$), reducing the interfacial energy will be the most effective way (compared to reducing E_a or enhancing supersaturation) to enhance the nucleation rate. Such sensitivity analyses reveal the relative importance of kinetic and thermodynamic factors, and can potentially guide prediction and optimization of systems where nucleation takes place.

Methods

Substrate preparation. Environmentally abundant quartz was used as the substrate for heterogeneous nucleation experiments. Atomically flat quartz substrates with a polished (100) plane (roughness <5 Å) were purchased from MTI Corporation. The substrates were cut into $1\ cm \times 1\ cm$ squares and cleaned by sonication in acetone, ethanol, isopropanol, and ultrapure ionized water (DI water, $18.2\ M\Omega\ cm^{-1}$) successively for 20 min each. Then they were soaked in a mixture of sulfuric acid and Nochromix® for 2 h to remove any remaining organic compounds. The substrates were then rinsed thoroughly with DI water and stored in DI water for experimental use. The cleaned substrates were scanned using AFM to ensure the cleanness of the surface.

Aqueous chemistry. To generate a supersaturated solution with respect to $CaCO_3$ at constant supersaturation, we used a flow-through system. A $NaHCO_3$ solution and a $CaCl_2$ solution were separately driven by two peristaltic pumps into a micromixer to create a supersaturated solution. Using Geochemist's Workbench (GWB, Release 8.0, RockWare, Inc.)[45] and the thermo_minteq database, we quantified the supersaturation of the mixed solution to be $IAP/K_{sp} = 10^{1.65}$ at 12, 25, and 31 °C. These conditions were chosen so that heterogeneous nucleation occurs within the experimentally detectable window of both GISAXS and AFM within a reasonable reaction time. More discussion about the choice of conditions for the GISAXS-AFM method is available in Supplementary Note 2. Homogeneous nuclei are much larger than heterogeneous nuclei and much less numerous (Fig. 4), and thus can be excluded during GISAXS and AFM data analysis. To quantify the aqueous supersaturation, the solubility product of calcite ($K_{sp} = 10^{-8.42}$ at 12 °C, $K_{sp} = 10^{-8.48}$ at 25 °C, and $K_{sp} = 10^{-8.52}$ at 31 °C) was used for calculation[45]. The mixed solution was also oversaturated with vaterite (see Supplementary Note 1), but was undersaturated with amorphous $CaCO_3$[36,46]. The supersaturated solution was then injected into our reaction cell (2 mL volume) at a volumetric flow rate of 5.6 mL min^{-1}. The top surface of a piece of quartz substrate on the bottom of the reaction cell was in contact with the freshly injected solution. Waste solution was exhausted
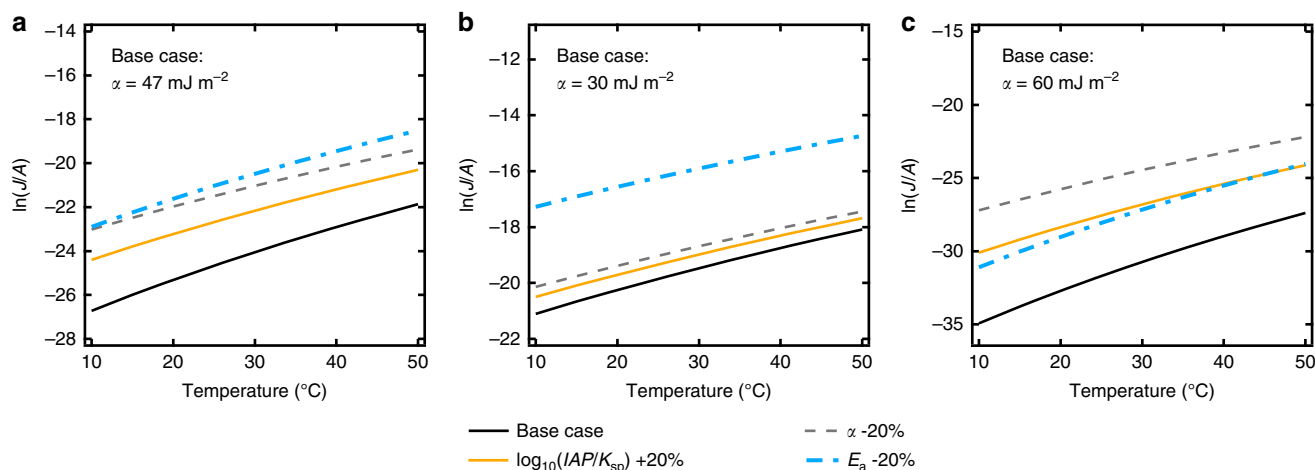
Fig. 6 Sensitivity analyses of nucleation rate for $CaCO_3$ nucleation on quartz. The variation in nucleation rates is manifested by plots of $\ln(J/A)$ as a function of temperature. Panel **a** shows the base case with $\alpha = 47\,mJ\,m^{-2}$, as for $CaCO_3$ nucleation on quartz, and panels **b** and **c** are for base cases with $\alpha = 30$ and $60\,mJ\,m^{-2}$, respectively. In all base cases, $\log_{10}(IAP/K_{sp}) = 1.65$, and $E_a = 45\,kJ\,mol^{-1}$. Increase in $\ln(J/A)$ is calculated with either 20% reduction in α, 20% increase in $\log_{10}(IAP/K_{sp})$, or 20% reduction in E_a, and is compared with the base case. (**a**) When $\alpha = 47\,mJ\,m^{-2}$, the nucleation rate at all temperatures is effectively enhanced by 20% variation in α, $\log_{10}(IAP/K_{sp})$, or E_a. (**b**) If $\alpha = 30\,mJ\,m^{-2}$, the nucleation rate is most effectively enhanced by a decrease in E_a. (**c**) If $\alpha = 60\,mJ\,m^{-2}$, a reduction in α will significantly increase the nucleation rate

from the top of the cell and collected for disposal. A diagram of the experimental setup is shown in Supplementary Figure 3.

To obtain the same supersaturation of the mixed solution at different temperatures, the concentration of $CaCl_2$ was tuned slightly to maintain a supersaturation fixed at $IAP/K_{sp} = 10^{1.65}$. The ratio of Ca/HCO_3^- was kept at 3.6–4.4 for all conditions, and the pH was within a 7.8–8.0 range. To control the system temperature, before mixing, the solutions of $CaCl_2$ and $NaHCO_3$ were either heated in the tubing using a heating plate, or cooled with a water/ice mixture. To minimize heat loss through tubing walls, the tubes after the temperature control component were covered with insulating foam. The temperature of each supersaturated solution was measured before and after the reaction at the inlet of the reaction cell, and the temperature fluctuation was less than 1 °C from the target value.

In situ GISAXS. In situ GISAXS data were collected at beamline 12-ID-B at the Advanced Photon Source (Argonne National Laboratory, USA). The reaction cell was aligned in the beamline. The front and back wall of the cell was made of Kapton film, allowing transmission of X-rays. A 14 keV X-ray beam (200 μm in width and 20 μm in height) incident onto the substrate at an angle of 0.11° (which gives a reflectivity of 98.8% for quartz) was scattered by particles on the substrate. The scattered X-rays were collected by a Pilatus 2M detector 2 m away from the sample, downstream of the beam. The scattering intensity from the particles on the quartz surface was obtained from in-plane cutting along the Yoneda wing in the same way as described in our previous studies[36]. After background subtract, the intensity (I) was plotted versus the scattering vector (q). The scattering vector is in the reciprocal space of the horizontal dimension of the particles, and was 0.008–0.4 $Å^{-1}$ in our setup. This corresponds to an observable particle's lateral radius range of 0.8–40 nm, well capturing the in-plane heterogeneous $CaCO_3$ nucleus radius which is usually several nanometers. Scattering with q values larger than 0.1 $Å^{-1}$ has low signal-to-noise ratios and is largely affected by background scattering, and therefore was not used for analyses. After obtaining the $I(q)$ plots, we used the conventional SAXS formula for further analyses, because the nucleus radius in our system (about 5 nm) is small enough ($R < 4.5\lambda/4\pi\alpha_i$) that the GISAXS-specific formula derived from distorted-wave Born approximation is not necessary[47]. The total volume of heterogeneously formed nuclei with radii within 3–30 nm was represented by invariant (Q), where $Q = \frac{1}{2\pi^2}\int I(q)q^2 dq$ for $q = 0.01–0.1\,Å^{-1}$ (refs. [36,39]). For a nucleation-dominant system where nucleus size does not change significantly, the invariant is proportional to the nucleus number, and can be treated as the total nucleus number with a relative unit comparable to all invariant values calculated in this study[48]. The invariant method can be applied to the samples with a signal-to-noise ratio too low to be fitted with the GISAXS fitting method.

For samples with relatively high signal-to-noise ratios, we fitted the GISAXS intensity according to[36,39,48,49]

$$I(q) = N \cdot \Delta\rho^2 \cdot \int D(R)V^2(R)P(q,R)dR \cdot \left[I_{pow}q^{-P} + S(q)\right], \quad (5)$$

where N is the nucleus number, $\Delta\rho$ is the difference of the scattering length density

between nuclei and the solution background, $D(R)$ is the nucleus size distribution, $V(R)$ is the volume of nuclei with an in-plane radius of R, and $P(q,R)$ is the form factor which in this case is written for spherical particles. The $I_{pow}q^{-P}$ term expresses the intensity contribution from large surfaces such as those of aggregates and large particles settled from solution. The structure factor $S(q)$ is equal to one for our dilute system. Because of the uncertainty of the properties of newly formed $CaCO_3$ nuclei in terms of water content and polymorphy, the absolute value of $\Delta\rho$ is hard to estimate, and is assumed constant and assigned a value of 1, yielding fitting results of N proportional to the actual particle numbers. Thus, the fitted N can be treated as particle numbers with a relative unit comparable to any fitted N values throughout this study[36]. The nucleus numbers obtained from the invariant method and fitting method are in different units, but are consistent with each other after linear scaling[36], as shown in Fig. 2. The rates of increases in the nucleus number (obtained from the fitting method) were recorded as nucleation rates, with relative units. The variation of these nucleation rates obtained at different temperatures was used to calculate the apparent activation energy, E_a.

Assuming a Schultz distribution $D(R)$ for a polydisperse system, the radius of gyration can be calculated as R_g. In our systems, the nucleus size did not vary significantly, which further justifies the idea that the invariant values that are proportional to the total nucleus volume are also proportional to the nucleus numbers.

Ex situ atomic force microscopy. To calibrate the nucleation rates in relative unites obtained with GISAXS with absolute nucleation rates, and to visually observe nanometer-scale nuclei, we complemented the GISAXS experiment with ex situ AFM experiments. The experiments were conducted as described in the GISAXS section, except that the reaction was ended at different time points. At each desired reaction time, the substrate was taken out of the cell. The residual reaction solution was immediately rinsed off with ethanol to end the reaction. Ethanol (100%) was used instead of water to minimize dissolution of $CaCO_3$ nuclei. The substrate was then dried with ultrapure nitrogen gas, and immediately scanned using AFM to minimize aging of the nuclei. Only the evenly distributed particles on the surface were counted to obtain the nuclei density (nuclei μm^{-2}), because even distribution occurs mainly in systems where epitaxial heterogeneous nucleation takes place on the substrate. The larger, randomly distributed particles were formed in solution and settled on the surface (i.e., homogeneously nucleated particles). The manually counted nucleus densities per unit area were used to calibrate the nucleation rate (r.u.) obtained with GISAXS. Tapping mode was used to collect images. AFM probes used in this study were purchased from Bruker (Model: RTESP, Part: MPP-11100-10). Because the AFM tip radius (8 nm) is comparable to the lateral nuclei radius, and because $CaCO_3$ nuclei might have experienced dehydration after the substrate was taken out of the reaction solution, we did not use AFM images to extract lateral nucleus sizes. In this study, AFM imaging provided only nuclei number densities on the substrate.

Data availability
The data sets supporting the current study are available from the corresponding author on reasonable request.

References

1. Li, Q. *Calcium Carbonate Formation in Energy-Related Subsurface Environments and Engineered Systems*. Doctor of Philosophy thesis, Washington University, St. Louis (2016).

2. Lindberg, C. et al. Silver as seed-particle material for GaAs nanowires—dictating crystal phase and growth direction by substrate orientation. *Nano Lett.* **16**, 2181–2188 (2016).

3. Thanh, N. T., Maclean, N. & Mahiddine, S. Mechanisms of nucleation and growth of nanoparticles in solution. *Chem. Rev.* **114**, 7610–7630 (2014).

4. Xia, Y., Xia, X. & Peng, H.-C. Shape-controlled synthesis of colloidal metal nanocrystals: thermodynamic versus kinetic products. *J. Am. Chem. Soc.* **137**, 7947–7966 (2015).

5. Wu, L. et al. High-temperature crystallization of nanocrystals into three-dimensional superlattices. *Nature* **548**, 197–201 (2017).

6. Zeng, J. et al. Gold-based hybrid nanocrystals through heterogeneous nucleation and growth. *Adv. Mater.* **22**, 1936–1940 (2010).

7. Pei, A., Zheng, G., Shi, F., Li, Y. & Cui, Y. Nanoscale nucleation and growth of electrodeposited lithium metal. *Nano Lett.* **17**, 1132–1139 (2017).

8. Lai, S. C., Lazenby, R. A., Kirkman, P. M. & Unwin, P. R. Nucleation, aggregative growth and detachment of metal nanoparticles during electrodeposition at electrode surfaces. *Chem. Sci.* **6**, 1126–1138 (2015).

9. Lau, S. & Archer, L. A. Nucleation and growth of lithium peroxide in the Li–O₂ battery. *Nano Lett.* **15**, 5995–6002 (2015).

10. Thomas, J. J., Jennings, H. M. & Chen, J. J. Influence of nucleation seeding on the hydration mechanisms of tricalcium silicate and cement. *J. Phys. Chem. C* **113**, 4327–4334 (2009).

11. Thomas, J. J. A new approach to modeling the nucleation and growth kinetics of tricalcium silicate hydration. *J. Am. Ceram. Soc.* **90**, 3282–3288 (2007).

12. Hu, Y., Lee, B., Bell, C. & Jun, Y.-S. Environmentally abundant anions influence the nucleation, growth, Ostwald ripening, and aggregation of hydrous Fe(III) oxides. *Langmuir* **28**, 7737–7746 (2012).

13. Hu, Y., Neil, C., Lee, B. & Jun, Y.-S. Control of heterogeneous Fe (III)(hydr) oxide nucleation and growth by interfacial energies and local saturations. *Environ. Sci. Technol.* **47**, 9198–9206 (2013).

14. Li, Q., Steefel, C. I. & Jun, Y.-S. Incorporating nanoscale effects into a continuum-scale reactive transport model for CO₂-deteriorated cement. *Environ. Sci. Technol.* **51**, 10861–10871 (2017).

15. Jun, Y.-S., Zhang, L., Min, Y. & Li, Q. Nanoscale chemical processes affecting storage capacities and seals during geologic CO₂ sequestration. *Acc. Chem. Res.* **50**, 1521–1529 (2017).

16. Chen, L., Jacquet, R., Lowder, E. & Landis, W. J. Refinement of collagen–mineral interaction: a possible role for osteocalcin in apatite crystal nucleation, growth and development. *Bone* **71**, 7–16 (2015).

17. Smeets, P. J., Cho, K. R., Kempen, R. G., Sommerdijk, N. A. & De Yoreo, J. J. Calcium carbonate nucleation driven by ion binding in a biomimetic matrix revealed by in situ electron microscopy. *Nat. Mater.* **14**, 394–339 (2015).

18. Hoang, T. A. in *Mineral* Scales *and Deposits* (ed. Amjad, Z.) Ch. 3, 47–83 (Elsevier B.V.; Amsterdam, Netherlands, 2015).

19. Zhao, J., Wang, M., Lababidi, H. M., Al-Adwani, H. & Gleason, K. K. A review of heterogeneous nucleation of calcium carbonate and control strategies for scale formation in multi-stage flash (MSF) desalination plants. *Desalination* **442**, 75–88 (2018).

20. Parambil, J. V., Poornachary, S. K., Tan, R. B. & Heng, J. Y. Template-induced polymorphic selectivity: the effects of surface chemistry and solute concentration on carbamazepine crystallisation. *CrystEngComm* **16**, 4927–4930 (2014).

21. Steefel, C. I. & Van Cappellen, P. A new kinetic approach to modeling water–rock interaction: the role of nucleation, precursors, and Ostwald ripening. *Geochim. Cosmochim. Acta* **54**, 2657–2677 (1990).

22. Ievlev, A. V. et al. Quantitative description of crystal nucleation and growth from in situ liquid scanning transmission electron microscopy. *ACS Nano* **9**, 11784–11791 (2015).

23. Zimmermann, N. E., Vorselaars, B., Quigley, D. & Peters, B. Nucleation of NaCl from aqueous solution: critical sizes, ion-attachment kinetics, and rates. *J. Am. Chem. Soc.* **137**, 13352–13361 (2015).

24. Poonoosamy, J. et al. Barite precipitation following celestite dissolution in a porous medium: a SEM/BSE and μ-XRD/XRF Study. *Geochim. Cosmochim. Acta* **182**, 131–144 (2016).

25. Hu, Q. et al. The thermodynamics of calcite nucleation at organic interfaces: classical vs. non-classical pathways. *Faraday Discuss.* **159**, 509–523 (2012).

26. De Yoreo, J. J. & Vekilov, P. G. Principles of crystal nucleation and growth. *Rev. Mineral Geochem.* **54**, 57–93 (2003).

27. Vehkämäki, H. *Classical Nucleation Theory in Multicomponent Systems* (Springer-Verlag Berlin Heidelberg; Germany, 2006).

28. Nielsen, A. E. *Kinetics of Precipitation* (Pergamon Press, Oxford, 1964).

29. Lasaga, A. C. *Kinetic Theory in the Earth Sciences* (Princeton University Press; Princeton, New Jersey, 1998).

30. Gebauer, D., Völkel, A. & Cölfen, H. Stable prenucleation calcium carbonate clusters. *Science* **322**, 1819–1822 (2008).

31. Baumgartner, J. et al. Nucleation and growth of magnetite from solution. *Nat. Mater.* **12**, 310–314 (2013).

32. Navrotsky, A. Energetic clues to pathways to biomineralization: precursors, clusters, and nanoparticles. *Proc. Natl. Acad. Sci. USA* **101**, 12096–12101 (2004).

33. Hamm, L. M. et al. Reconciling disparate views of template-directed nucleation through measurement of calcite nucleation kinetics and binding energies. *Proc. Natl. Acad. Sci. USA* **111**, 1304–1309 (2014).

34. Fernandez-Martinez, A., Hu, Y., Lee, B., Jun, Y.-S. & Waychunas, G. A. In situ determination of interfacial energies between heterogeneously nucleated CaCO₃ and quartz substrates: thermodynamics of CO₂ mineral trapping. *Environ. Sci. Technol.* **47**, 102–109 (2013).

35. Giuffre, A. J., Hamm, L. M., Han, N., De Yoreo, J. J. & Dove, P. M. Polysaccharide chemistry regulates kinetics of calcite nucleation through competition of interfacial energies. *Proc. Natl. Acad. Sci. USA* **110**, 9261–9266 (2013).

36. Li, Q., Fernandez-Martinez, A., Lee, B., Waychunas, G. A. & Jun, Y.-S. Interfacial energies for heterogeneous nucleation of calcium carbonate on mica and quartz. *Environ. Sci. Technol.* **48**, 5745–5753 (2014).

37. De Yoreo, J. J., Waychunas, G. A., Jun, Y.-S. & Fernandez-Martinez, A. In situ investigations of carbonate nucleation on mineral and organic surfaces. *Rev. Mineral. Geochem.* **77**, 229–257 (2013).

38. Tarasevich, Y. I. Surface energy of oxides and silicates. *Theor. Exp. Chem.* **42**, 145–161 (2006).

39. Jun, Y.-S., Kim, D. & Neil, C. W. Heterogeneous nucleation and growth of nanoparticles at environmental interfaces. *Acc. Chem. Res.* **49**, 1681–1690 (2016).

40. Kim, D., Lee, B., Thomopoulos, S. & Jun, Y.-S. In situ evaluation of calcium phosphate nucleation kinetics and pathways during intra- and extrafibrillar mineralization of collagen matrices. *Cryst. Growth Des.* **16**, 5359–5366 (2016).

41. Kim, D., Lee, B., Thomopoulos, S. & Jun, Y.-S. The role of confined collagen geometry in decreasing nucleation energy barriers to intrafibrillar mineralization. *Nat. Commun.* **9**, 962 (2018).

42. Wallace, A. F., DeYoreo, J. J. & Dove, P. M. Kinetics of silica nucleation on carboxyl- and amine-terminated surfaces: insights for biomineralization. *J. Am. Chem. Soc.* **131**, 5244–5250 (2009).

43. Schwartzkopf, M. et al. Real-time monitoring of morphology and optical properties during sputter deposition for tailoring metal–polymer interfaces. *ACS Appl. Mater. Interfaces* **7**, 13547–13556 (2015).

44. Kalikmanov, V. in *Nucleation Theory* 17–41 (Science+Business Media Dordrecht; Dordrecht, Netherlands, 2013).

45. Bethke, C. & Yeakel, S. *The Geochemist's Workbench®, Version 8.0. Hydrogeology Program* (University of Illinois, Urbana, 2009).

46. Brečević, L. & Nielsen, A. E. Solubility of amorphous calcium carbonate. *J. Cryst. Growth* **98**, 504–510 (1989).

47. Lee, B. et al. Structural characterization using the multiple scattering effects in grazing-incidence small-angle X-ray scattering. *J. Appl. Crystallogr.* **41**, 134–142 (2008).

48. Jun, Y.-S., Lee, B. & Waychunas, G. A. In situ observations of nanoparticle early development kinetics at mineral−water interfaces. *Environ. Sci. Technol.* **44**, 8182–8189 (2010).

49. Narayanan, T. in *Applications of Synchrotron Light to Scattering and Diffraction in Materials and Life Sciences*. Vol. 776: Lecture Notes in *Physics* (eds Gomez, M., Nogales, A., Garcia-Gutierrez, M. C. & Ezquerra, T. A.) Ch. 6, 133–156 (Springer, Berlin, Heidelberg, 2009).

Acknowledgements

Author contributions

Y.-S.J. directed the research. Q.L. contributed on data collection and analyses. Q.L. and Y.-S.J. contributed to writing the manuscript.

Additional information

Supplementary information accompanies this paper at https://doi.org/10.1038/s42004-018-0056-5.

Competing interests: The authors declare no competing interests.

Reprints and permission information is available online at http://npg.nature.com/reprintsandpermissions/

Publisher's note: Springer Nature remains neutral with regard to jurisdictional claims in published maps and institutional affiliations.